Progress In Electromagnetics Research C, Vol. 89, 61–74, 2019

Electroquasistatic Model of Capacitive Hyperthermia Affected by Heat Convection

Chien-Chang Chen and Jean-Fu Kiang*

Abstract—An electroquasistatic (EQS) model of capacitive hyperthermia for treating lung tumors is proposed, based on which the finite element method is applied to compute the electrical potential in a human thorax model. The temperature distribution in the thorax model, which is surrounded by a bolus maintained at a constant temperature, is computed by numerically solving a bio-heat equation, which includes metabolic heat generated in the tissues, heat convection mechanism in tissues and bolus, as well as the heat delivered by the microwave field computed with the EQS model and finite element method. Temperature-dependent blood perfusion rates of blood and muscle, respectively, are adopted to account for the physiological reaction of tissues to temperature variation. By simulations, it is observed that adjusting the dielectric properties of adipose tissue via injection, the time evolution of temperature distribution can be controlled to some extent, providing more flexibility to customize a hyperthermia treatment plan for specific patient.

1. INTRODUCTION

Hyperthermia (HT) treatment was conducted by delivering RF power to a malignant tumor to raise its temperature up to 40–46°C [1] over a period of 50 minutes [2]. Typically, the local temperature surrounding the treated region is maintained under 44°C to avoid collateral damages, and the body temperature is maintained below 42°C to make the patient feel comfortable. Different types of HT techniques have been proposed, including capacitive [3], inductive [4], phased array [5], ultrasound [6] and interstitial [7]. Typical operating frequencies include 1–300 MHz in the RF band and 300 MHz–300 GHz in the microwave band [8]; 5 kHz–1 MHz for inductive HT [8], 5–430 MHz for capacitive HT [9], and 70–2,450 MHz for phased-array HT [10].

If the dimension of the treated region is comparable to one wavelength, full-wave methods should be applied to compute the electric-field distribution in that region [11]. Examples of full-wave methods include finite-difference time-domain (FDTD) method [12, 13], finite element method (FEM) [4], finite integration technique [11], and so on. If the dimension of the treated region is much smaller than one wavelength, quasistatic approximation should be used instead [14].

Thermal models have been used to compute the temperature distribution in tissues, including the cooling mechanism of perfusion [15, 16]. The tissue was modeled as continuous medium [17], porous medium [18] or with the WJL (Weinbaum, Jiji and Lemon) model [18]. A discrete vessel model was proposed to account for large blood vessels in determining the local temperature distribution [15]. Spatial and time variation of arterial blood temperature can be incorporated to simulate physiological phenomenon [19]. A network model of straight vessels has also been used [16].

In applying the hyperthermia technique, the tumor degradation process can be modeled with an Arrhenius-type kinetic equation [19]. Cell apoptosis in different cell phases appears different. The cells in S-phase and M-phase undergo a slow mode of cell death after hyperthermia [1]. The cells in G1-phase

Received 25 September 2018, Accepted 8 December 2018, Scheduled 20 December 2018
* Corresponding author: Jean-Fu Kiang (jfkiang@ntu.edu.tw).
The authors are with the Graduate Institute of Communication Engineering, National Taiwan University, Taipei 106, Taiwan.

appear relatively heat resistant and reveal no microscopic damage during the exposure to heat, but may follow a rapid mode of death immediately after hyperthermia [1]. In this work, cell apoptosis during the 50-minute treatment period is neglected.

The heat convection between human body and water bolus depends on the thermal properties and thickness of the latter [12]. The temperature distribution in the tissues has been computed with FEM [20], boundary element method (BEM) [21], Monte Carlo method [22] and time-space decoupled form [23].

Before applying capacitive HT on a specific patient, the position of electrodes should be adjusted to acquire a better deep-heating pattern [3]. Other clinic factors may also affect the practice of HT, including treatment planning, design of applicators [13], metal implants [14] and the use of magnetite [24]. In principle, an effective treatment plan requires the optimization of temperature distribution in the treated region while avoiding collateral hot spots in the other tissues [15].

In this work, an electroquasistatic (EQS) model is proposed to compute the potential distribution induced in a human thorax model when RF power is delivered via a pair of electrodes. The distribution of specific absorption rate (SAR) is then derived, followed by the Pennes' bio-heat equation and convective heat equation to compute the temperature distribution in the thorax [3]. The cooling effect of water bolus surrounding the skin and the modulation of dielectric properties in adipose tissues are also discussed.

This paper is organized as follows. The formulation and numerical scheme to compute the electric potential distribution in a three-dimensional thorax model are presented in Section 2. The bio-heat equation and numerical scheme to compute the temperature distribution are presented in Section 3, and the simulation results are discussed in Section 4. Finally, some conclusions are drawn in Section 5.

2. FIELD DISTRIBUTION IN THORAX MODEL

Figure 1 shows the schematic of thorax model, where the human body in prone position is modeled as a tube with elliptical cross-section, each lung modeled as an ellipsoid, and the tumor modeled as a sphere. Fig. 2 shows the schematic of the ribs, sternum and spine, which are superimposed to the model in Fig. 1 in the simulations.

In the electroquasistatic (EQS) scheme, the zeroth-order electric potential $\Phi^{(0)}(\bar{r})$ satisfies

$$\nabla \cdot \left[\epsilon(\bar{r})\nabla\Phi^{(0)}(\bar{r})\right] = -\rho^{(0)}(\bar{r}) \tag{1}$$

where $\rho^{(0)}(\bar{r})$ (C/m^3) is the zeroth-order charge density in the thorax model. To apply the finite element method, the whole thorax model is first decomposed into a finite set of tetrahedra, and the scalar potential distribution in the thorax model is expanded in terms of the scalar Whitney-0 form elements $\{\lambda_n(\bar{r})\}$ as [25, 26]

$$\Phi^{(0)}(\bar{r}) = \sum_{n=1}^{N_v} \phi_n^{(0)} \lambda_n(\bar{r}) \tag{2}$$

where $\lambda_n(\bar{r})$ is a linear function of x, y and z within a tetrahedron, and N_v is the total number of vertices. Next, substitute Eq. (2) into Eq. (1) and apply the Petrov-Galerkin procedure [26] by multiplying $\lambda_m(\bar{r})$ to both sides of Eq. (1) then integrating over the domain of $\lambda_m(\bar{r})$ to obtain a matrix equation

$$\bar{\bar{S}} \cdot \bar{\phi}^{(0)} = \bar{b}_s \tag{3}$$

where $\bar{\bar{S}}$ is a coefficient matrix, with $S_{mn} = \iiint d\bar{r}\lambda_m(\bar{r})\nabla\cdot[\epsilon(\bar{r})\nabla\lambda_n(\bar{r})]$; $\bar{\phi}^{(0)}$ contains the zeroth-order electrical potentials at all the vertices; and $\bar{b}_s$ is derived from the potentials imposed on the electrodes, with $b_{sm} = -\iiint d\bar{r}\lambda_m(\bar{r})\rho(\bar{r})$. A preconditioned generalized minimal residual (GMRES) method is then applied to solve Eq. (3) for $\bar{\phi}^{(0)}$ [27].

The arrangement of electrodes as shown in Fig. 1 makes the zeroth-order current $\bar{J}^{(0)}(\bar{r}) = 0$ negligible, which implies that $\bar{A}^{(0)}(\bar{r}) = 0$ and $\bar{H}^{(0)}(\bar{r}) = 0$. Hence, the electric field can be represented only in terms of $\Phi^{(0)}(\bar{r})$ as

$$\bar{E}^{(0)}(\bar{r}) = -\nabla\Phi^{(0)}(\bar{r})$$

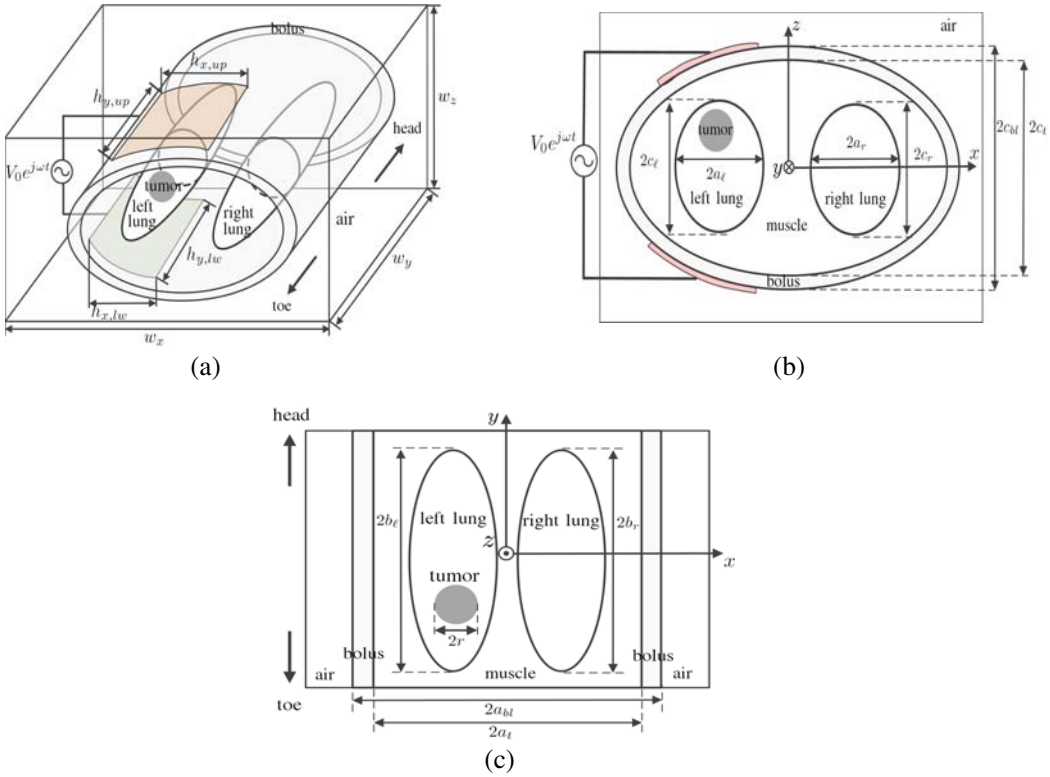

Figure 1. Schematic of thorax model, (a) panoramic view, (b) xz cross-section and (c) xy cross-section.

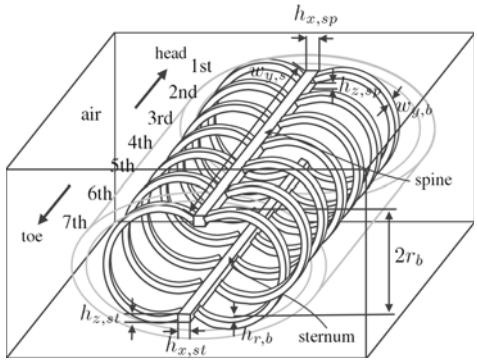

Figure 2. Schematic of ribs, sternum and spine.

which induces a first-order current to drive a first-order magnetic vector potential $\bar{A}^{(1)}(\bar{r})$ as

$$\nabla \times \left[\frac{1}{\mu(\bar{r})}\nabla \times \bar{A}^{(1)}(\bar{r})\right] = j\omega\epsilon(\bar{r})\bar{E}^{(0)}(\bar{r}) \tag{4}$$

The magnetic vector potential $\bar{A}^{(1)}(\bar{r})$ is then expanded in terms of the vector Whitney-1 form elements $\{\bar{\omega}_n(\bar{r})\}$ as [25, 26]

$$\bar{A}^{(1)}(\bar{r}) = \sum_{n=1}^{N_e} a_n \bar{\omega}_n(\bar{r}) \tag{5}$$

where $\bar{\omega}_n(\bar{r})$ has unit tangential component over the assigned edge of a tetrahedron, and N_e is the total number of edges. By substituting Eq. (5) into Eq. (4) and applying the Petrov-Galerkin procedure to Eq. (4), a matrix equation is derived as

$$\bar{\bar{K}}_1 \cdot \bar{a}^{(1)} = \bar{b}_k$$

where $\bar{\bar{K}}_1$ is another coefficient matrix; $\bar{a}^{(1)}$ contains the first-order magnetic vector potential along all the edges; and $\bar{b}_k$ is derived from the displacement current term on the right-hand side of Eq. (4). The GMRES is then applied to solve for $\bar{A}^{(1)}(\bar{r})$.

By neglecting the first-order electric charge in the thorax model, the first-order electric field is computed as

$$\bar{E}^{(1)}(\bar{r}) = -j\omega\bar{A}^{(1)}(\bar{r})$$

The validity of applying the EQS approach can be confirmed by checking if

$$\left|\bar{E}^{(0)}(\bar{r})\right| \gg \left|\bar{E}^{(1)}(\bar{r})\right|$$

The full-wave solution $\bar{E}(\bar{r})$ [25] will also be used to confirm the EQS approach.

The power density per unit volume can be represented as [3]

$$Q_{\rm em}(\bar{r}) = \frac{\sigma(\bar{r})}{2}\left|\bar{E}^{(0)}(\bar{r})\right|^2 \ (\text{Watt/m}^3)$$

where $\sigma(\bar{r})$ is the conductivity (S/m) of the tissues, and the specific absorption rate (SAR) is computed as

$$\text{SAR}(\bar{r}) = \frac{Q_{\rm em}(\bar{r})}{\rho(\bar{r})}$$

where $\rho(\bar{r})$ (kg/m^3) is the mass density of the tissues.

3. TEMPERATURE DISTRIBUTION IN THORAX MODEL

The temperature distribution in the thorax model satisfies the bio-heat equation [28]

$$\rho(\bar{r})c(\bar{r})\frac{\partial T(\bar{r},t)}{\partial t} = \nabla\cdot[\zeta(\bar{r})\nabla T(\bar{r},t)] - \xi(\bar{r})\rho(\bar{r})\rho_b c_b\left[T(\bar{r},t) - T_b\right] + Q_s(\bar{r},t) \tag{6}$$

where $c(\bar{r})$ (J/kg/K) is the heat capacity of the tissues; ρ_b and c_b are the mass density and heat capacity, respectively, of blood; $\zeta(\bar{r})$ (Watt/m/K) and $T(\bar{r},t)$ (K) are the thermal conductivity and temperature, respectively, of the tissues; $\xi(\bar{r})$ (m^3/kg/s) is the blood flow rate per-unit-mass of tissues; T_b is the temperature of blood, which is approximated as a constant; and $Q_s(\bar{r},t)$ (Watt/m^3) is the heat source, which is composed of

$$Q_s(\bar{r},t) = Q_{\rm em}(\bar{r},t) + Q_{\rm met}(\bar{r},t)$$

where $Q_{\rm met}(\bar{r},t)$ (Watt/m^3) is the metabolic heat generation.

By applying the Crank-Nicholson scheme [29] to (6), with $\partial T(\bar{r},t)/\partial t \simeq [T(\bar{r},t+\Delta t) - T(\bar{r},t)]/\Delta t$, $T(\bar{r},t) \simeq [T(\bar{r},t+\Delta t) + T(\bar{r},t)]/2$ and $Q_s(\bar{r},t) \simeq [Q_s(\bar{r},t+\Delta t) + Q_s(\bar{r},t)]/2$, a time-domain finite-difference equation is obtained as

$$\begin{aligned}\rho(\bar{r})c(\bar{r})\frac{T(\bar{r},t+\Delta t)-T(\bar{r},t)}{\Delta t} =& \nabla\cdot\left[\zeta(\bar{r})\nabla\left(\frac{T(\bar{r},t+\Delta t)+T(\bar{r},t)}{2}\right)\right] \\ & - \xi(\bar{r})\rho(\bar{r})\rho_b c_b\left[\frac{T(\bar{r},t+\Delta t)+T(\bar{r},t)}{2} - T_b\right] + \frac{Q_s(\bar{r},t+\Delta t)+Q_s(\bar{r},t)}{2}\end{aligned} \tag{7}$$

Next, the temperature distribution is expanded as a superposition of scalar Whitney-0 form elements as [25, 26]

$$T(\bar{r},t) = \sum_{n=1}^{N_v} b_n(t)\lambda_n(\bar{r}) \tag{8}$$

By substituting Eq. (8) into Eq. (7), we obtain

$$\begin{aligned}\sum_{n=1}^{N_v}\rho(\bar{r})c(\bar{r})\lambda_n(\bar{r})\left(\frac{b_n(t+\Delta t)-b_n(t)}{\Delta t}\right) =& \sum_{n=1}^{N_v}\left\{\nabla\cdot[\zeta(\bar{r})\nabla\lambda_n(\bar{r})] - \xi(\bar{r})\rho(\bar{r})\rho_b c_b\lambda_n(\bar{r})\right\} \\ & \left\{\frac{b_n(t+\Delta t)}{2} + \frac{b_n(t)}{2}\right\} + \frac{Q_s(\bar{r},t+\Delta t)+Q_s(\bar{r},t)}{2} + \xi(\bar{r})\rho(\bar{r})\rho_b c_b T_b\end{aligned} \tag{9}$$

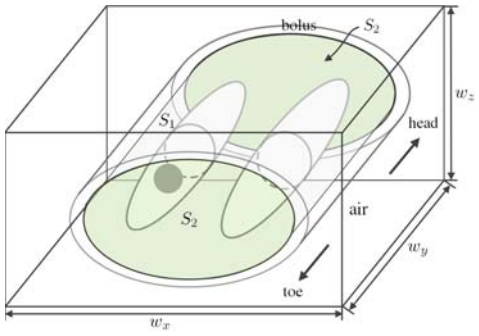

Figure 3. Schematic of thorax model to compute temperature distribution.

Figure 3 shows the schematic of thorax model to compute the temperature distribution, where S_1 is an elliptic tubular surface between the tissue and the bolus, and S_2 are two elliptic cross-sections attached to the end of S_1, indicating the junction between the tissue and the computational domain. The volume enclosed by $S_1 + S_2$ is labeled as V. By multiplying $\lambda_m(\bar{r})$, with $1 \leq m \leq N_v$, to both sides of Eq. (9) then integrating over V, we have

$$\begin{aligned}
&\sum_{n=1}^{N_v} \frac{b_n(t+\Delta t) - b_n(t)}{\Delta t} \iiint_V d\bar{r}\rho(\bar{r})c(\bar{r})\lambda_m(\bar{r})\lambda_n(\bar{r}) \\
&= \sum_{n=1}^{N_v} \frac{b_n(t+\Delta t) + b_n(t)}{2} \left[\iint_{S_1+S_2} d\bar{a}\cdot\zeta(\bar{r})\lambda_m(\bar{r})\nabla\lambda_n(\bar{r}) \right. \\
&\quad - \iiint_V d\bar{r}\zeta(\bar{r})\nabla\lambda_m(\bar{r})\cdot\nabla\lambda_n(\bar{r}) - \left. \iiint_V d\bar{r}\xi(\bar{r})\rho(\bar{r})\rho_b c_b \lambda_m(\bar{r})\lambda_n(\bar{r}) \right] \\
&\quad + \iiint_V d\bar{r}\lambda_m(\bar{r}) \left[\frac{Q_s(\bar{r}, t+\Delta t) + Q_s(\bar{r}, t)}{2} + \xi(\bar{r})\rho(\bar{r})\rho_b c_b T_b \right]
\end{aligned} \tag{10}$$

The heat convection across S_1 is characterized by

$$\hat{n}\cdot\zeta(\bar{r})\nabla T(\bar{r}, t) = -\alpha\left[T(\bar{r}, t) - T_0\right], \quad \bar{r} \in S_1,\ t \geq 0 \tag{11}$$

where $\hat{n}$ is a unit normal vector pointing outwards from S_1; α (Watt/m^2/K) is the heat transfer coefficient between tissues and bolus; and T_0 (K) is the temperature of bolus, which is assumed constant. By substituting Eq. (8) into Eq. (11), we have

$$\hat{n}\cdot\sum_{n=1}^{N_v}\zeta(\bar{r})b_n(t)\nabla\lambda_n(\bar{r}) = \alpha\left[T_0 - \sum_{n=1}^{N_v} b_n(t)\lambda_n(\bar{r})\right] \tag{12}$$

By multiplying $\lambda_m(\bar{r})$, with $1 \leq m \leq N_v$, to both sides of Eq. (12) then integrating over S_1, we have

$$\sum_{n=1}^{N_v} b_n(t) \iint_{S_1} d\bar{a}\cdot\zeta(\bar{r})\lambda_m(\bar{r})\nabla\lambda_n(\bar{r}) = \iint_{S_1} da\lambda_m(\bar{r})\alpha T_0 - \sum_{n=1}^{N_v} b_n(t) \iint_{S_1} da\alpha\lambda_m(\bar{r})\lambda_n(\bar{r}) \tag{13}$$

Assume there is no heat flowing through S_2, namely,

$$\hat{n}\cdot\zeta(\bar{r})\nabla T(\bar{r}, t) = 0, \quad \bar{r} \in S_2,\ t \geq 0 \tag{14}$$

By substituting Eq. (8) into Eq. (14), we have

$$\hat{n}\cdot\sum_{n=1}^{N_v}\zeta(\bar{r})b_n(t)\nabla\lambda_n(\bar{r}) = 0 \tag{15}$$

By multiplying $\lambda_m(\bar{r})$, with $1 \le m \le N_v$, to both sides of Eq. (15) then integrating over S_2, we have

$$\sum_{n=1}^{N_v} b_n(t) \iint_{S_2} d\bar{a} \cdot \zeta(\bar{r}) \lambda_m(\bar{r}) \nabla \lambda_n(\bar{r}) = 0 \tag{16}$$

By substituting Eqs. (13) and (16) into Eq. (10), we obtain a matrix equation

$$\left(\bar{\bar{U}} + \bar{\bar{V}}\right) \cdot \bar{b}(t + \Delta t) = \left(\bar{\bar{U}} - \bar{\bar{V}}\right) \cdot \bar{b}(t) + \bar{d} \tag{17}$$

where

$$\begin{aligned}
U_{mn} &= \frac{1}{\Delta t} \iiint_V d\bar{r} \rho(\bar{r}) c(\bar{r}) \lambda_m(\bar{r}) \lambda_n(\bar{r}) \\
V_{mn} &= \frac{1}{2} \left[\iint_{S_1} d\bar{a} \alpha \lambda_m(\bar{r}) \lambda_n(\bar{r}) + \iiint_V d\bar{r} \zeta(\bar{r}) \nabla \lambda_m(\bar{r}) \cdot \nabla \lambda_n(\bar{r}) + \iiint_V d\bar{r} \xi(\bar{r}) \rho(\bar{r}) \rho_b c_b \lambda_m(\bar{r}) \lambda_n(\bar{r}) \right] \\
d_m &= \iiint_V d\bar{r} \lambda_m(\bar{r}) \left[\frac{Q_s(\bar{r}, t + \Delta t) + Q_s(\bar{r}, t)}{2} + \xi(\bar{r}) \rho(\bar{r}) \rho_b c_b T_b \right] + \iint_{S_1} d\bar{a} \lambda_m(\bar{r}) \alpha T_0 \\
\bar{b}(t) &= [b_1(t), b_2(t), \ldots, b_{N_v}(t)]^t
\end{aligned}$$

The GMRES is then applied to solve Eq. (17) for the time evolution of temperature distribution.

4. SIMULATIONS AND DISCUSSIONS

Table 1 lists the geometrical parameters of the thorax model [30] used in the simulations. The size of the three-dimensional computational domain is specified as (w_x, w_y, w_z). A tumor is located in the lower posterior of the left lobe. The semi-axes of an ellipsoid are labeled as a, b and c in x, y and z directions, respectively, and subscripts ℓ, r, t and bl stand for left lung, right lung, torso and bolus, respectively. Two rectangular electrodes of size $h_x \times h_y$ are placed conformally to the bolus surface, and subscripts up and lw indicate the upper and lower electrodes, respectively. Each rib is modeled as a circular arc of radius r_b, with the rib thickness $h_{r,b}$ in the radial direction and width $w_{y,b}$ in the y direction. Both the spine and the sternum are approximated to have rectangular cross-section, with widths of h_x and h_z in x and z directions, respectively; and subscripts sp and st indicate spine and sternum, respectively. The length of both spine and sternum within the computational domain is $w_{y,s}$. To simplify the coding scheme, the sternum length is increased by about 3 cm, and the arc length of the first rib is also increased. The average thickness of subcutaneous fat tissue in the thorax model ranges from 0.5 to 2.5 cm for male and 1.5 to 4.0 cm for female [31]. It was reported that excessive heating could be induced in the subcutaneous fat which was thicker than 1.5–2 cm [9]. In this work, the thickness of subcutaneous fat tissue is set to 1 cm unless specified otherwise [9].

In [30], circular electrodes with diameter of 13 cm and 22 cm, respectively, were used, with surface areas of 132 cm^2 and 380 cm^2, respectively. In this work, the surface areas of the upper and the lower (rectangular) electrodes are set to 153.6 cm^2 and 500 cm^2, respectively. In [30], a thermometer was inserted 5 cm beneath the skin to measure the local temperature throughout the HT treatment. In this work, the lung tumor is located 6 cm beneath the skin.

Table 2 lists the electrical properties of the thorax model. The dielectric properties of bolus are adjusted to match those of muscles [28]. The dielectric properties of human muscle were measured at body temperature within 24 to 48 hours postmortem [32]. The dielectric properties of ovine cortical bone, measured at 37°C, are used to approximate those of human bones. The dielectric properties of lung tissue and tumor were measured at 8 MHz, 30 minutes after the tissue was removed from the human body, at temperature of 37°C and relative humidity above 90%. The conductivity and dielectric constant of the tumor tissue are higher than those of normal tissues [1].

Obvious difference of $|\epsilon|$ between bolus and adipose significantly reduces the electric field from penetrating into the torso. Provided that certain viable solution can be injected into the adipose layer and permeate around it during the HT treatment, the electrical conductivity of adipose can be increased to induce more electric current in muscle, lung and tumor. Furthermore, if the dielectric properties of tissues in between the two electrodes can be modulated in a similar manner, more power may be delivered

Table 1. Geometrical parameters of thorax model (in cm).

	size	position
left lung	$(2a_\ell, 2b_\ell, 2c_\ell) = (8, 22, 16)$	$(-6, 0, 0)$
right lung	$(2a_r, 2b_r, 2c_r) = (10, 22, 16)$	$(5, 0, 0)$
tumor	$2r = 4$	$(-6, -5, 4)$
computational domain	$(w_x, w_y, w_z) = (50, 36, 40)$	-
torso	$(2a_t, w_y, 2c_t) = (30, 36, 22)$	-
bolus	$(2a_{bl}, w_y, 2c_{bl}) = (34, 36, 26)$	-
upper electrode	$(h_{x,up}, h_{y,up}) = (12, 12)$	$(-6, -5, 12.2)$
lower electrode	$(h_{x,lw}, h_{y,lw}) = (20, 20)$	$(-6, -5, -12.2)$
1st left rib	$h_{r,b} = 1,\ w_{y,b} = 1\ r_b = 8$	$(-6, 8.5, 0)$
2nd left rib		$(-6, 5.5, 0)$
3rd left rib		$(-6, 2.5, 0)$
4th left rib		$(-6, -0.5, 0)$
5th left rib		$(-6, -3.5, 0)$
6th left rib		$(-6, -6.5, 0)$
7th left rib		$(-6, -9.5, 0)$
1st right rib	$h_{r,b} = 1,\ w_{y,b} = 1\ r_b = 8$	$(-6, 8.5, 0)$
2nd right rib		$(-6, 5.5, 0)$
3rd right rib		$(-6, 2.5, 0)$
4th right rib		$(-6, -0.5, 0)$
5th right rib		$(-6, -3.5, 0)$
6th right rib		$(-6, -6.5, 0)$
7th right rib		$(-6, -9.5, 0)$
spine	$h_{x,sp} = 2,\ h_{z,sp} = 2,\ w_{y,s} = 17$	$(0, 0, 7)$
sternum	$h_{x,st} = 2,\ h_{z,st} = 1,\ w_{y,s} = 17$	$(0, 0, -6.5)$

Table 2. Electrical properties of thorax model (at 8 MHz).

	ϵ_r	σ (S/m)	ϵ (F/m)
air	1	0	ϵ_0
bolus	172	0.69	$(172 - j1,552)\epsilon_0$
fat	13.7 [32]	0.0245 [32]	$(13.7 - j55.1)\epsilon_0$
bone	39 [32]	0.045 [32]	$(39 - j101)\epsilon_0$
muscle	172 [32]	0.69 [32]	$(172 - j1,552)\epsilon_0$
lung	264.9 [33]	0.42 [33]	$(264.9 - j945)\epsilon_0$
tumor	402 [33]	0.68 [33]	$(402 - j1,530)\epsilon_0$

to the tumor. Potential materials to increase the electrical conductivity include nanoparticles [34] and saline water [35]. In treating liver tissue of rabbits with RF ablation [35], hypertonic saline (36% NaCl) was injected to decrease the electrical impedance η of liver tissue from 116.3 Ω to 73 Ω, where

$$\eta = \sqrt{\frac{\mu}{\epsilon}} = \sqrt{\frac{\mu}{\epsilon_0 \left[\epsilon_r - j\sigma/(\omega\epsilon_0)\right]}} \tag{18}$$

which implies that σ is increased by about 2.5 times (at 8 MHz). Alternatively, solution containing nano-

particles was used to increase the electrical conductivity of local tissues by less than 10% in capacitive hyperthermia [34].

Figure 4(a) shows the original (unmodulated) case where the adipose with $(\epsilon, \sigma) = (13.7,\ 0.0245)$ is marked in light-blue, and the two electrodes are marked by thick curves. Figs. 4(b) and 4(c) show two modulating cases, where the modulated adipose with $(\epsilon, \sigma) = (13.7, 0.0245 \times 2.5)$ is marked in blue, and the modulated muscle with $(\epsilon, \sigma) = (172, 0.69 \times 2.5)$ is marked in orange. In case 1, a liposuction operation was performed in the adipose area near the electrodes, where the upper region falls in $x \in [-14, 2],\ y \in [-14, 6],\ z \in [4, 10]$ (in cm) and the lower region falls in $x \in [-16, 4],\ y \in [-14, 6],\ z \in [-10, -2]$ (in cm). Both regions laterally extend beyond the electrodes. The muscle within 1 cm below the adipose is also assumed to be modulated by the saline water. In case 2, less saline water is injected below the lower electrode, making the muscle below it unmodulated.

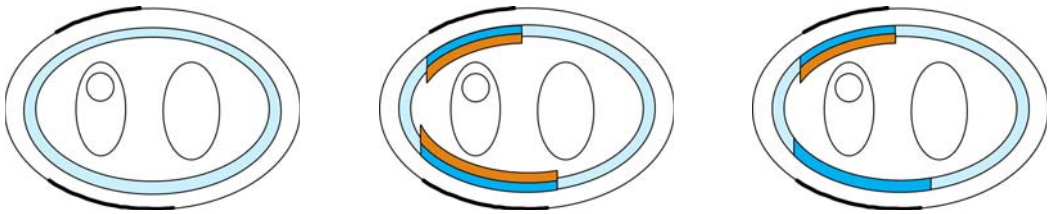

(a) (b) (c)

Figure 4. Schematic of modulating the conductivity of adipose and muscle, xz plane at $y = y_{\text{tumor}}$, (a) unmodulated case, (b) case 1 and (c) case 2.

Table 3 lists the thermal properties of the thorax model. In normal lung tissue, typical blood perfusion rate is 401 (ml/kg/min) or $\xi = 6.68 \times 10^{-6}$ (m^3/kg/s) [40], which is also adopted in [39]. The blood perfusion rate in a lung tumor, measured with multidetector computer tomography (MDCT) on patients with non-small cell lung cancer, is about 10.6 (ml/100 ml/min) [42] or 2.53×10^{-6} (m^3/kg/s), assuming the density of lung tumor is 697 (kg/m^3) [41]. During a typical hyperthermia treatment, ξ of tumor does not decrease as the temperature is raised up to 44°C [43]. In this work, it is approximated as a constant. The temperature-dependent blood perfusion rate of fat (ξ_{fat}) and muscle (ξ_{muscle}) are modeled as [44]

$$\xi_{\text{muscle}} = \begin{cases} 4.41 \times 10^{-7} + 3.48 \times 10^{-6} e^{-(T-45)^2/12}, & T \le 45 \\ 3.92 \times 10^{-6}, & T > 45 \end{cases}$$

$$\xi_{\text{fat}} = \begin{cases} 4.00 \times 10^{-7} + 4.00 \times 10^{-7} e^{-(T-45)^2/12}, & T \le 45 \\ 8.00 \times 10^{-7}, & T > 45 \end{cases}$$

where T is the temperature in °C.

The frequency of the voltage source connected to the electrodes is 8 MHz; the output power is 300 Watt; the magnitude of voltage on the upper electrode is 81.25 V; and the lower electrode is

Table 3. Thermal properties of thorax model.

	ζ (Watt/m/K)	ρ (kg/m^3)	c (J/kg/K)	ξ (m^3/kg/s)	Q_{met} (Watt/m^3)
fat	0.34 [36]	900 [28]	2,300 [28]	ξ_{fat}	5 [37]
bone	0.436 [28]	1,790 [28]	1,300 [28]	0.167×10^{-6} [38]	0 [39]
torso	0.50 [36]	1,020 [28]	3,500 [28]	ξ_{muscle}	4,200 [3]
lung	0.40 [36]	394 [40]	3,886 [20]	6.68×10^{-6} [40]	1,700 [20]
tumor	0.39 [20]	697 [41]	3,886 [20]	2.53×10^{-6} [42]	8,000 [20]
blood	-	1,000 [20]	4,180 [20]	-	-

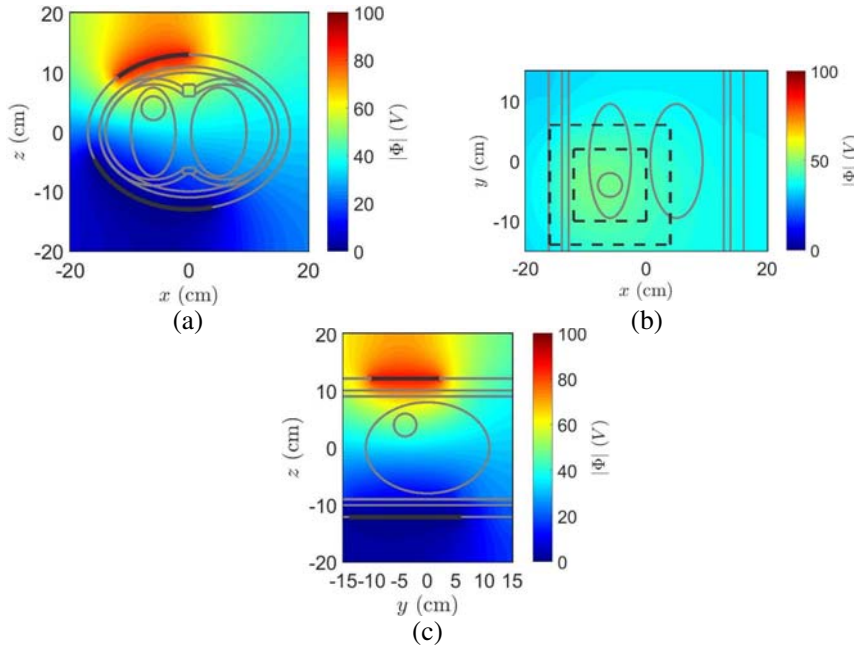

Figure 5. Distributions of potential in case 1, output power is 300 Watt, (a) xz plane, (b) xy plane and (c) yz plane.

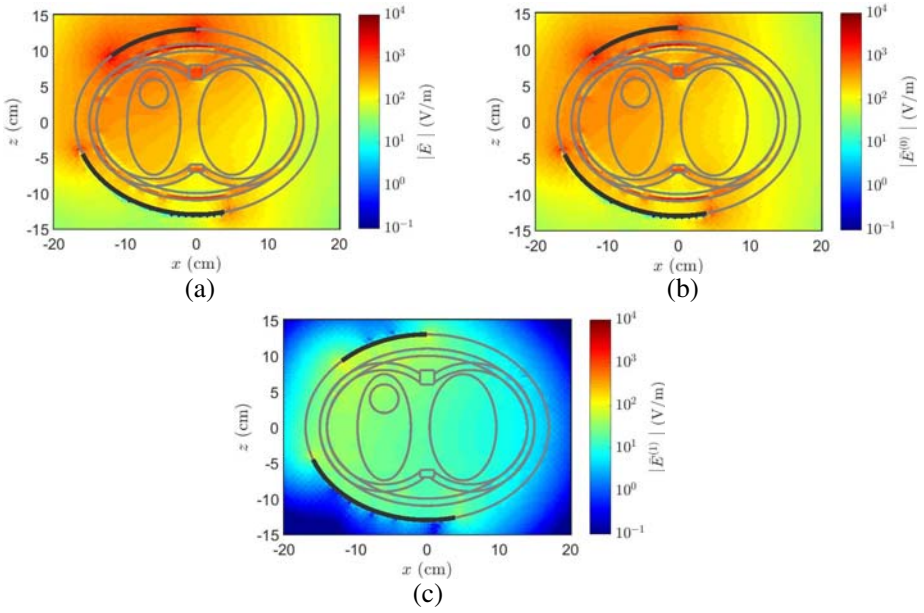

Figure 6. Magnitude of electric field in case 1, magnitude of voltage source is 86.97 V, (a) full-wave solution, (b) zeroth-order solution and (c) first-order solution.

grounded. The volume of each tetrahedron is about 0.02 cm^3. Fig. 5 shows the potential distributions in the thorax model of case 1. The electrodes are marked by black arcs in Figs. 5(a) and 5(c), and the projections of both electrodes are marked by dashed rectangles in Fig. 5(b).

Figure 6 shows the magnitude of electric fields in the xz plane of case 1, with the magnitude of voltage source as 86.97 V. The full-wave, zeroth-order and first-order solutions are presented. The magnitudes of electric field within the tumor region are $|\bar{E}| = 413\,\mathrm{V/m}$, $|\bar{E}^{(0)}| = 365\,\mathrm{V/m}$ and

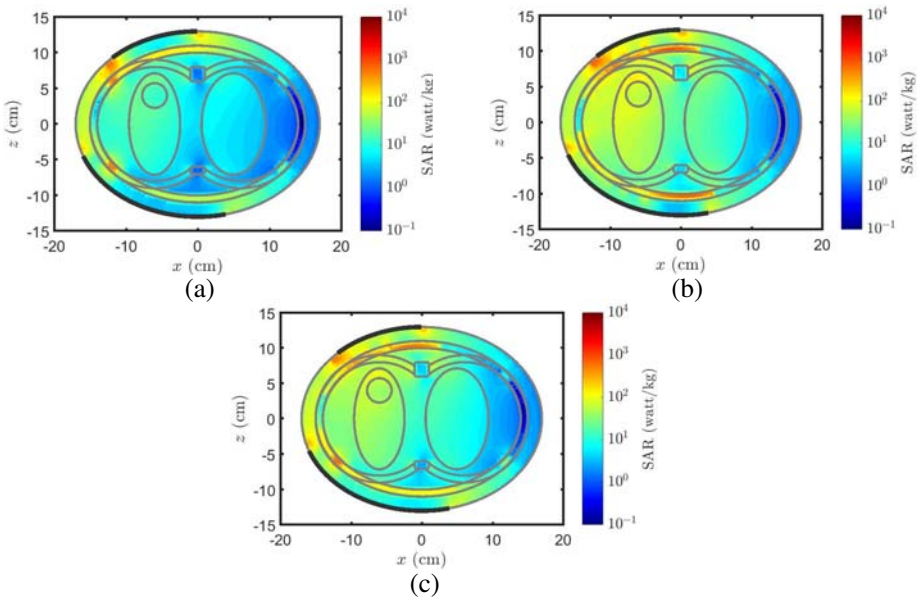

Figure 7. Distributions of SAR in xz plane at $y = y_{\text{tumor}}$, source voltage is 86.97 V, (a) original case, (b) case 1 and (c) case 2.

$|\bar{E}^{(1)}| = 35\,\text{V/m}$, respectively. The first-order field is an order of magnitude smaller than the full-wave field and the zeroth-order field, implying that the EQS approximation provides sufficiently accurate results at 8 MHz.

Figure 7 shows the SAR distributions in the original case where the adipose and the muscle tissue are not modulated in conductivity, as well as two other cases where the conductivity is locally modulated. The bones have relatively higher mass density than the surrounding tissues and have lower SAR value than the latter. The adipose tissue impedes the RF power from entering the torso. The SAR level inside the lungs is relatively high, due to its relatively low mass density ($242.6\,\text{kg/m}^3$). The SAR level is higher in the upper part than in the lower part because the upper electrode has a smaller size and the power is more focused around it than around the lower electrode. The SAR level increases near the edges of both electrodes because the electric field near the edge is enhanced. The SAR level is higher in the left side than in the right side because both electrodes are placed closer to the left side. High SAR level is observed in the adipose layer, and an obvious difference in SAR level appears around the adipose-muscle interface.

After liposuction operation on both upper and lower parts of torso, more RF power can penetrate into internal tissues. A reduction of around 0.5 cm adipose tissue can help prevent local hot-spots. Compared with case 2, additional saline water is injected below the lower electrode in case 1, hence the penetrating RF power is increased from 259 Watt in case 2 to 300 Watt in case 1, with the upper electrode applied the same voltage and the lower electrode grounded. The SAR levels at the center of the tumor in the unmodulated case, case 1 and case 2 are 13, 60 and 58 (Watt/kg), respectively. The EM heat source in case 1 is $Q_{\text{em}} \simeq 42,000$ (Watt/m^3), and that in a reference case [21] is $Q_{\text{em}} \simeq 22,600$ (Watt/m^3).

Table 4 lists the operational parameters during different phases of an HT treatment plan in [30]. The same RF power will be applied in simulating the original case and case 2.

Figure 8 shows the time variation of tumor temperature by applying continuous wave during the 50-minute treatment period, simulated at time intervals of $\Delta t = 15\,\text{s}$. The nonlinear ξ is updated at time instants of 1, 2, 3, 4, 5, 7, 10, 15, 25 and 35 minutes, respectively, after the initiating time. In case 1 and case 2, the temperature of tumor is raised from 36°C at $t = 0$ to 41.7°C at $t = 50$ minutes. As a reference, the temperature in a clinic case [30] rises from 36°C at $t = 0$ to 45°C at $t = 50$ minutes.

Figure 9 shows the temperature distributions at $t = 50$ minutes in the original case, case 1 and case 2, respectively. The temperature near the tissue-bolus interface is kept low by the bolus. The

Table 4. Operational parameters of HT treatment plan in case 1.

time (min.)	voltage (V)	current (A)	power (Watt)
0–5	79.39	6.30	250
5–35	84.02	6.67	280
35–50	86.97	6.90	300

temperature around the upper electrode is raised higher in all three cases. Due to low value of ξ in the tumor, its temperature can reach 39.19°C (original case), 41.63°C (case 1) and 41.78°C (case 2), respectively, which is higher than its surrounding tissues. However, the temperature at hot-spot can reach 59.5°C, 43.69°C and 46.79°C, respectively. Additional modulation of conductivity around the lower electrode may help reduce the hot-spot temperature. This study demonstrates possible effect on the temperature distribution by modulating the conductivity near the hot-spots, in terms of field theory and heat-convection mechanism. The physiological effects and other clinic issues need further study, which are out of the scope of this work.

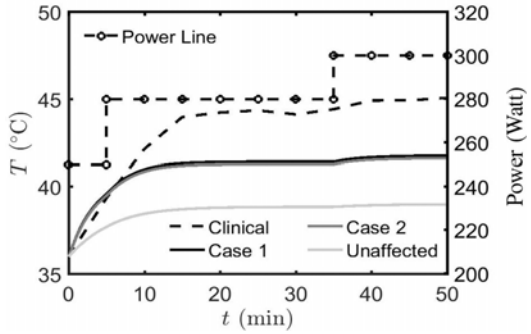

Figure 8. Tumor temperature: − − −: clinical result [30], ———: this work; − ∘ −: output power.

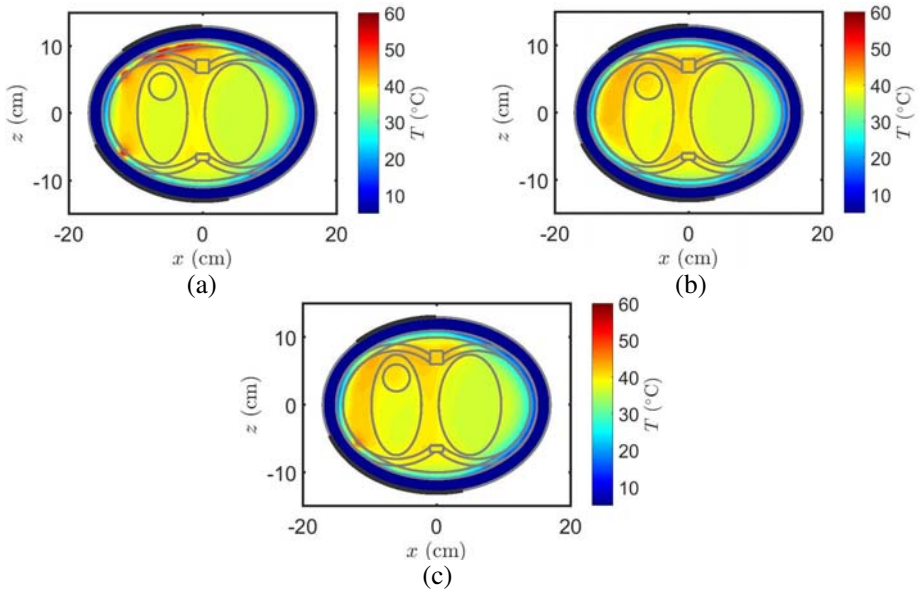

Figure 9. Distributions of temperature at $t = 50$ minutes in the xz plane at $y = y_{\text{tumor}}$, (a) original case, (b) case 1 and (c) case 2.

5. CONCLUSION

An EQS model of capacitive hyperthermia for treating lung tumor is proposed, which is followed by applying the finite element method to compute the electrical potential in a human thorax model. The temperature distribution is computed by numerically solving a bio-heat equation, including metabolic heat and heat convection in tissues as well as microwave power delivered from the capacitive electrodes. Simulation results indicate that by injecting saline water to modulate the conductivity in adipose and muscle tissues, more microwave power can be delivered to raise the tumor temperature.

ACKNOWLEDGMENT

This work is partly sponsored by the Ministry of Science and Technology, Taiwan, under contract MOST 106-2221-E-002-014 and partly supported by the donation from Pixart Imaging Inc. for promoting science and technology.

REFERENCES

1. Hegyi, G., G. P. Szigeti, and A. Szász, "Hyperthermia versus oncothermia: Cellular effects in complementary cancer therapy," *Evidence-Based Complementary Alternative Medicine*, Vol. 2013, 672873, Jan. 2013.
2. Ohguri, T., K. Yahara, S. D. Moon, S. Yamaguchi, H. Imada, H. Terashima, and Y. Korogi, "Deep regional hyperthermia for the whole thoracic region using 8 MHz radiofrequency-capacitive heating device: Relationship between the radiofrequency-output power and the intra-oesophageal temperature and predictive factors for a good heating in 59 patients," *Int. J. Hyperthermia*, Vol. 27, No. 1, 20–26, Feb. 2011.
3. Jamil, M. and E. Y. K. Ng, "To optimize the efficacy of bioheat transfer in capacitive hyperthermia: A physical perspective," *J. Therm. Biol.*, Vol. 38, No. 5, 272–279, Jul. 2013.
4. Kotsuka, Y., H. Kayahara, K. Murano, H. Matsui, and M. Hamuro, "Local inductive heating method using novel high-temperature implant for thermal treatment of luminal organs," *IEEE Trans. Microwave Theory Tech.*, Vol. 57, No. 10, 2574–2580, Oct. 2009.
5. Kowalski, M. E. and J.-M. Jin, "Model-based optimization of phased arrays for electromagnetic hyperthermia," *IEEE Trans. Microwave Theory Tech.*, Vol. 52, No. 8, 1964–1977, Aug. 2004.
6. Staruch, R., R. Chopra, and K. Hynynen, "Hyperthermia in bone generated with MR imaging controlled focused ultrasound: Control strategies and drug delivery," *Radiology*, Vol. 263, No. 1, 117–127, Apr. 2012.
7. Chen, X., C. J. Diederich, J. H. Wootton, J. Pouliot, and I.-C. Hsu, "Optimisation-based thermal treatment planning for catheter-based ultrasound hyperthermia," *Int. J. Hyperthermia*, Vol. 26, No. 1, 39–55, Feb. 2010.
8. Szasz, A., O. Szasz, and N. Szasz, "Physical background and technical realizations of hyperthermia," *Hyperthermia in Cancer Treatment: A Primer*, G. F. Baronzio and E. D. Hager, ed., Medical Intelligence Unit, 2006.
9. Hiraoka, M., M. Mitsumori, N. Hiroi, S. Ohno, Y. Tanaka, Y. Kotsuka, and K. Sugimachi, "Development of RF and microwave heating equipment and clinical application to cancer treatment in Japan," *IEEE Trans. Microwave Theory Tech.*, Vol. 48, No. 11, 1789–1799, Nov. 2000.
10. Tao, Y.-H. and G. Wang, "Conformal hyperthermia of superficial tumor with left-handed metamaterial lens applicator," *IEEE Trans. Biomed. Eng.*, Vol. 59, No. 12, 3525–3530, Dec. 2012.
11. Hand, J. W., "Modelling the interaction of electromagnetic fields (10 MHz-10 GHz) with the human body: Methods and applications," *Phys. Med. Biol.*, Vol. 53, R243–R286, 2008.
12. Aghayan, S. A., D. Sardari, S. R. M. Mahdavi, and M. H. Zahmatkesh, "Estimation of overall heat transfer coefficient of cooling system in RF capacitive hyperthermia," *J. Biomed. Sci. Eng.*, Vol. 6, No. 5, 509–517, 2013.

13. Kok, H. P., M. de Greef, N. van Wieringen, D. Correia, M. C. C. M. Hulshof, P. J. Zum VöRde Sive VöRding, J. Sijbrands, A. Bel, and J. Crezee, "Comparison of two different 70 MHz applicators for large extremity lesions: Simulation and application," *Int. J. Hyperthermia*, Vol. 26, No. 4, 376–388, Jun. 2010.
14. Kato, H., M. Kondo, H. Imada, M. Kuroda, Y. Kamimura, K. Saito, K. Kuroda, K. Ito, H. Takahashi, and H. Matsuki, "Quality assurance: Recommended guidelines for safe heating by capacitive-type heating technique to treat patients with metallic implants," *Int. J. Hyperthermia*, Vol. 29, No. 2, 99–105, Feb. 2013.
15. Kok, H. P., P. Wust, P. R. Stauffer, F. Bardati, G. C. van Rhoon, and J. Crezee, "Current state of the art of regional hyperthermia treatment planning: A review," *Radiation Oncology*, Vol. 10, No. 196, Sep. 2015.
16. Kok, H. P., J. Gellermann, C. A. T. van den Berg, P. R. Stauffer, J. W. Hand, and J. Crezee, "Thermal modelling using discrete vasculature for thermal therapy: A review," *Int. J. Hyperthermia*, Vol. 29, No. 4, 336–345, Jun. 2013.
17. Kim, K., T. Seo, K. Sim, and Y. Kwon, "Magnetic nanoparticle-assisted microwave hyperthermia using an active integrated heat applicator," *IEEE Trans. Microwave Theory Tech.*, Vol. 64, No. 7, 2184–2197, Jul. 2016.
18. Hassanpour, S. and A. Saboonchi, "Interstitial hyperthermia treatment of countercurrent vascular tissue: A comparison of Pennes, WJ and porous media bioheat models," *J. Therm. Biol.*, Vol. 46, 47–55, Dec. 2014.
19. Dombrovsky, L. A., V. Timchenko, and M. Jackson, "Indirect heating strategy of laser induced hyperthermia: An advanced thermal model," *Int. J. Heat Mass Transfer*, Vol. 55, Nos. 17–18, 4688–4700, Aug. 2012.
20. Astefanoaei, I., I. Dumitru, H. Chiriac, and A. Stancu, "Use of the Fe-Cr-Nb-B systems with low Curie temperature as mediators in magnetic hyperthermia," *IEEE Trans. Magn.*, Vol. 50, No. 11, 7400904, Nov. 2014.
21. Jamil, M. and E. Y. K. Ng, "The modelling of heating a tissue subjected to external electromagnetic field," *Acta Bioeng. Biomech.*, Vol. 10, No. 2, 29–37, 2008.
22. Lv, Y.-G., Z.-S. Deng, and J. Liu, "3-D numerical study on the induced heating effects of embedded micro/nanoparticles on human body subject to external medical electromagnetic field," *IEEE Trans. Nanobiosci.*, Vol. 4, No. 4, 284–294, Dec. 2005.
23. Zhong, J.-Q., S. Liang, Y.-P. Yuan, and Q. Y. Xiong, "Coupled electromagnetic and heat transfer ODE model for microwave heating with temperature-dependent permittivity," *IEEE Trans. Microwave Theory Tech.*, Vol. 64, No. 8, 2467–2477, Aug. 2016.
24. Kawai, N., D. Kobayashi, T. Yasui, Y. Umemoto, K. Mizuno, A. Okada, K. Tozawa, T. Kobayashi, and K. Kohri, "Evaluation of side effects of radiofrequency capacitive hyperthermia with magnetite on the blood vessel walls of tumor metastatic lesion surrounding the abdominal large vessels: An agar phantom study," *Vascular Cell*, Vol. 6, No. 15, Jul. 2014.
25. Li, Y.-L., S. Sun, Q. I. Dai, and W. C. Chew, "Finite element implementation of the generalized-Lorenz gauged A-Φ formulation for low-frequency circuit modeling," *IEEE Trans. Antennas Propagat.*, Vol. 64, No. 10, 4355–4364, Jul. 2016.
26. Zhu, Y. and A. C. Cangellaris, *Multigrid Finite Element Methods for Electromagnetic Field Modeling*, Wiley-IEEE Press, 2006.
27. Barrett, R., M. Berry, T. F. Chan, J. Demmel, J. M. Donato, J. Dongarra, V. Eijkhout, R. Pozo, C. Romine, and H. van der Vorst, *Templates for the Solution of Linear Systems: Building Blocks for Iterative Methods*, SIAM, Philadelphia, 1994.
28. Tsuda, N., K. Kuroda, and Y. Suzuki, "An inverse method to optimize heating conditions in RF-capacitive hyperthermia," *IEEE Trans. Biomed. Eng.*, Vol. 43, No. 10, 1029–1037, 1996.
29. Sadiku, M. N. O., *Numerical Techniques in Electromagnetics*, 2nd Edition, Chap. 3, Finite Difference Method, CRC Press, Jul. 2000.
30. Abe, M., M. Hiraoka, M. Takahashi, S. Egawa, C. Matsuda, Y. Onoyama, K. Morita, M. Kakehi, and T. Sugahara, "Multi-institutional studies on hyperthermia using an 8-MHz radiofrequency

capacitive heating device (Thermotron RF-8) in combination with radiation for cancer therapy," *Cancer*, Vol. 58, No. 8, 1589–1595, Oct. 1986.

31. Holcombe, S. A. and S. C. Wang, "Subcutaneous fat distribution in the human torso," *Int. Res. Council Biomechanics Injury*, 389–396, 2014.
32. Gabriel, S., R. W. Lau, and C. Gabriel, "The dielectric properties of biological tissues: II. Measurements in the frequency range 10 Hz to 20 GHz," *Phys. Med. Biol.*, Vol. 41, No. 11, 2251–2269, Nov. 1996.
33. Wang, H.-X., J.-R. Wang, B.-Y. Sun, S. P., X. Xu, and Q. Su, "Experimental study of dielectric properties of human lung tissue in vitro," *J. Med. Biol. Eng.*, Vol. 34, No. 6, 598–604, 2014.
34. Kim, K. S. and S. Y. Lee, "Nanoparticle-mediated radiofrequency capacitive hyperthermia: A phantom study with magnetic resonance thermometry," *Int. J. Hyperthermia*, Vol. 31, No. 8, 831–839, Nov. 2015.
35. Lee, J. M., Y. K. Kim, Y. H. Lee, S. W. Kim, C. A. Li, and C. S. Kim, "Percutaneous radiofrequency thermal ablation with hypertonic saline injection: In vivo study in a rabbit liver model," *Korean J. Radiol.*, Vol. 4, No. 1, 27–34, Jan.–Mar. 2003.
36. Choi, J.-H., M. Morrissey, and J. C. Bischof, "Thermal processing of biological tissue at high temperatures: Impact of protein denaturation and water loss on the thermal properties of human and porcine liver in the range 25–80°C," *J. Heat Transfer*, Vol. 135, No. 6, 061302, May 2013.
37. Wilson, S. B. and V. A. Spence, "A tissue heat transfer model for relating dynamic skin temperature changes to physiological parameters," *Phys. Med. Biol.*, Vol. 33, No. 8, 895–912, Feb. 1988.
38. Itis.ethz.ch, "Tissue properties database V3.1," 2016, https://itis.swiss/virtual-population/tissue-properties/downloads/database-v3-1/.
39. Bernardi, P., M. Cavagnaro, S. Pisa, and E. Piuzzi, "Specific absorption rate and temperature elevation in a subject exposed in the far-field of radio-frequency sources operating in the 10–900 MHz range," *IEEE Trans. Biomed. Eng.*, Vol. 50, No. 3, 295–304, 2003.
40. Zorbas, G. and T. Samaras, "Simulation of radiofrequency ablation in real human anatomy," *Int. J. Hyperthermia*, Vol. 30, No. 8, 570–578, Dec. 2014.
41. Ye, J. C., J. H. Chang, Z. Q. Li, A. G. Wernicke, D. Nori, and B. Parashar, "Tumor density, size, and histology in the outcome of stereotactic body radiation therapy for early-stage non-small-cell lung cancer: A single-institution experience," *Ann. Meeting Am. Radium Soc.*, Apr. 2015.
42. Ng, Q. S., V. Goh, E. Klotz, H. Fichte, M. I. Saunders, P. J. Hoskinl, and A. R. Padhani, "Quantitative assessment of lung cancer perfusion using MDCT: Does measurement reproducibility improve with greater tumor volume coverage?," *Am. J. Roentgenol.*, Vol. 187, No. 4, 1079–1084, Oct. 2006.
43. Rossmann, C. and D. Haemmerich, "Review of temperature dependence of thermal properties, dielectric properties, and perfusion of biological tissues at hyperthermic and ablation temperatures," *Crit. Rev. Biomed. Eng.*, Vol. 42, No. 6, 467–492, 2014.
44. Lang, J., B. Erdmann, and M. Seebass, "Impact of nonlinear heat transfer on temperature control in regional hyperthermia," *IEEE Trans. Biomed. Eng.*, Vol. 46, No. 9, 1129–1138, Sep. 1999.